Coarse-to-Fine Hamiltonian Dynamics of Hierarchical Flows in Computational Anatomy

Michael I. Miller
Johns Hopkins University
Baltimore, Maryland, USA
mim@jhu.edu

Daniel J. Tward
Johns Hopkins University
3400 N. Charles St., Baltimore, MD 21218
dtward@cis.jhu.edu

Alain Trouvé
Ecole Normale Superieure
45 Rue d'Ulm, 75005 Paris, France
trouve@cmla.ens-cachan.fr

Abstract

We present here the Hamiltonian control equations for hierarchical diffeomorphic flows of particles. We define the controls to be a series of multi-scale vector fields, each with their own reproducing kernel Hilbert space norm. The hierarchical control is connected across scale through successive refinements that refine as they ascend the hierarchy with commensurately higher bandwidth Green's kernels. Interestingly the geodesic equations do not separate, with fine scale motions determined by all of the particle information simultaneously, from coarse to fine. Additionally, the hierarchical conservation law is derived, defining the geodesics and demonstrating the constancy of the Hamiltonian. We show results on one simulated example and one example from histological images of an Alzheimer's disease brain. We introduce the varifold action to transport the weights of micro-scale particles for mapping to sub millimeter scale cortical folds.

1. Introduction

This paper specifically focuses on a hierarchical representation of diffeomorphic flows for computational anatomy. Our motivation is to accommodate the multiple scales represented, from cellular scale to meso-scale [5, 14] to millimeter [11] anatomical scales of the numerous brain mapping projects in which we are involved. Most current methods in computational anatomy focus on deformable brain atlases that are built from imaging data at a single scale (typically millimeter resolution clinical MRI). These atlases are mapped to new datasets using deformations regularized with smooth kernels at a single scale (typically a few millimeters to centimeters). In contrast, our current experimental work in Alzheimer's disease is mapping the micro scales of molecular Tau-pathology measured via histology, to the sub-millimeter scales of anatomy obtained via moderate and high field MRI [13]. Towards this end we derive a set of Hamiltonian control equations that allow us to directly model information across scales resulting from molecular and anatomical imaging.

There have been many successful approaches in the 80's and 90's for representing multi-scale data, as well as many methods for the construction of scale-space. Our representation is abstract enough that it accommodates linear and non-linear transformations including wavelets [3, 6] and scattering functions [7] and multi-resolution pyramids for signal decomposition [1, 2]. We model the controls in our control system as being successively refined as the representation descends from the coarsest continuum scales of gross anatomy to the discrete, atom-like scales of cellular descriptions.

We have been motivated by other work on multi-scale kernels, [10, 12, 15, 4, 9] although our representation differs in that these multiple scale flows are not composed, rather they exist simultaneously with one another. The fact that the tangent space at the identity is successively refined via a sequence of vector fields corresponding to the higher and higher dimension of the finer scales, implies that the flow itself supports multiple information flows simultaneously. These scales are not decoupled.

2. Shapespace as an Orbit of Varifolds

Our shapes are is built via a series of generalized functions or measures spatially localized $\delta_{x_i}, x_i \in \mathbb{R}^3$, $i \in I$ with associated function represented by the parameter space

$f_i \in \mathcal{F}$. For us the function represents the amount of protein or Tau tangle at micro-scale in Alzheimer's disease for example. The mathematical model of Shapespace we use is termed *mathematical varifold measures*, representing mixtures of particles given by

$$\mu = \sum_{i \in I} w_i \delta_{x_i} \otimes \delta_{f_i} \, . \tag{1}$$

Shapespace is modeled as an infinite dimensional space, generated from one or more exemplars of varifolds $\mu = \sum_i w_i \delta_{x_i} \otimes \delta_{f_i}$ acted upon via the diffeomorphism group of one-to-one, onto maps, $\varphi = (\varphi_1, \varphi_2, \varphi_3) \in \text{Diff}$ (e.g. 3 components for 3 dimensional images) with diffeomorphic action given by

$$\varphi \cdot \mu := \sum_{i \in I} w_i |d\varphi(x_i)| \delta_{\varphi(x_i)} \otimes \delta_{f_i} \, . \tag{2}$$

We use varifolds and their action because they are an efficient way to transport a functional feature unchanged.

The diffeomorphisms are generated from vector fields indexed by time $t \to u_t = (u_{t1}, u_{t2}, u_{t3})$ and integrated to generate the flows

$$\dot{\varphi}_t = u_t \circ \varphi_t, \; \varphi_0 = \text{id} \, . \tag{3}$$

They extend the singular molecular varifolds of Shapespace, to the dense macro-scale continuum of cellular or particle descriptions, to global tissue scales (for example).

3. Shapespace as a Hierarchical Dynamical System with Metric

Our model is a hierarchical one in which we define a hierarchy of varifolds $\boldsymbol{\mu} = (\mu^{(\ell)})_{\ell \in L}$ and diffeomorphisms $\boldsymbol{\varphi} = (\varphi^{(\ell)})_{\ell \in L}$, each corresponding to their own flow and having their action. The group becomes $G = \prod_{\ell \in L} \text{Diff}_0^k(\mathbb{R}^d)$ with composition of each component and action componentwise on the varifolds, where for any L-uplets $\boldsymbol{\varphi} = (\varphi^{(\ell)})_{\ell \in L}$ and $\boldsymbol{\psi} = (\psi^{(\ell)})_{\ell \in L}$

$$\boldsymbol{\varphi} \cdot \boldsymbol{\psi} = (\varphi^{(\ell)} \circ \psi^{(\ell)})_{\ell \in L} \, , \tag{4a}$$

with the extended action of (2) becoming

$$\boldsymbol{\varphi} \cdot \boldsymbol{\mu} = (\varphi^{(\ell)} \cdot \mu^{(\ell)})_{\ell \in L} \, . \tag{4b}$$

The entire space of varifolds we call Shapespace, which is an orbit $\mathcal{M} = \{\boldsymbol{\varphi} \cdot \boldsymbol{\mu} : \varphi \in G\}$ generated from the varifold particle models across all scales.

We represent our model as a hierarchical dynamical system, the vector fields u are the controls on the flows satisfying Eqn. (3). This is depicted in Figure 1. We define the states of our dynamical system to encode the flows of

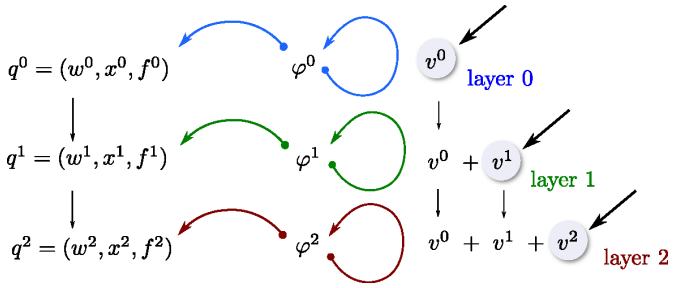

Figure 1: Hierarchical dynamical system with states q^ℓ, controls successively refined $u^\ell = \sum_i v^i$ and flows φ^ℓ.

the varifolds at each level. We define the associated state process of our dynamical system $t \mapsto q_t = (q_t^\ell)_{\ell \in L}$ to encode the varifold action of (2), $q_{ti} = (w_{ti}, x_{ti}, f_i)_{i \in I}$ $w_{ti} = |d\varphi_t(x_i)| w_i$ and $x_{ti} = \varphi_t(x_i)$, with state velocity linear in the control $t \mapsto u_t$:

$$\dot{q}_{ti} = (w_{ti} \text{div} u_t(x_{ti}), u_t(x_{ti}), 0) \, . \tag{5}$$

The layers in the hierarchy are coupled since the controlling vector fields u^ℓ are determined by successive refinements v^ℓ, for $\ell = 0, 1, \ldots$:

$$u^\ell = u^{\ell-1} + v^\ell \, , \; u^0 = v^0 \, , \; \ell = 1, \ldots \, . \tag{6}$$

We make the Shapespace into a metric space by examining the measures using a measure norm. However, in order to accomodate arbitrary scale into the dense continuum limit we build the underlying space of shapes into a metric space by measuring within the dense space of diffeomorphic motions on the backround space in which the particles are embedded. This way, we always have a metric independent of the scale at which we look at the problem.

To measure the length of the mappings of one shape to another we use the distance on the diffeomorphism group

$$d(\boldsymbol{\mu}, \boldsymbol{\mu}') = \inf_{\varphi : \boldsymbol{\varphi} \cdot \boldsymbol{\mu} = \boldsymbol{\mu}'} d_{Diff}(id, \boldsymbol{\varphi}) \, , \tag{7a}$$

with the length metric on diffeomorphisms

$$d_{Diff}^2(id, \boldsymbol{\psi}) = \inf_{\substack{\boldsymbol{u} : \dot{\boldsymbol{\varphi}}_t = \boldsymbol{u}_t \circ \boldsymbol{\varphi}_t \\ \boldsymbol{\varphi}_0 = id, \boldsymbol{\varphi}_1 = \boldsymbol{\psi}}} \int_0^1 \sum_\ell \| \boldsymbol{u}_t^\ell - \boldsymbol{u}_t^{\ell-1} \|_{V^\ell}^2 dt \, . \tag{7b}$$

4. Hamiltonian Control

For building correspondences from one varifold to aonther we measure closeness between varifolds $\boldsymbol{\mu} = (\mu^\ell)_{\ell \in L}, \boldsymbol{\mu}' = (\mu'^\ell)_{\ell \in L} \in \mathcal{M}$ via the measure norm

$\|\boldsymbol{\mu} - \boldsymbol{\mu}'\|_{\mathcal{M}}$. The measure norm is defined by calculating the integrals of the measures against test functions $h \to \boldsymbol{\mu}(h) = \int h(x)\boldsymbol{\mu}(dx)$ defined by

$$\|\boldsymbol{\mu}\|_{\mathcal{M}} := \sup_{h:\|h\|=1} |\boldsymbol{\mu}(h)| \,. \tag{8}$$

At every scale of the hierarchy the norm has two kernels, one for space and one for function, K_S^ℓ and $K_{\mathcal{F}}^\ell$ (resp. on $\mathbb{R}^d$ and $\mathcal{F}^\ell$) induced by the dot product

$$\langle \delta_x \otimes \delta_f, \delta_{x'} \otimes \delta_{f'} \rangle = K_S^\ell(x,x') K_F^\ell(f,f') \,. \tag{9}$$

Take the index union $K^\ell = J^\ell \cup J'^\ell$ of points and features then the difference of measures becomes

$$\begin{aligned} \mu^\ell - \mu'^\ell &= \sum_{j\in J^\ell} w_j \delta_{x_j} \otimes \delta_{f_j} - \sum_{j\in J'^\ell} w'_j \delta_{x'_j} \otimes \delta_{f'_j} \\ &= \sum_{k\in K^\ell} \alpha_k \delta_{\tilde{x}_k} \otimes \delta_{\tilde{f}_k} \end{aligned} \tag{10}$$

with norm-square

$$\|\mu^\ell - \mu'^\ell\|^2_{\mathcal{M}} = \sum_{k,k'\in K^\ell} \alpha_k \alpha_{k'} K_S^\ell(\tilde{x}_k, \tilde{x}_{k'}) K_F^\ell(\tilde{f}_k, \tilde{f}_{k'}) \,. \tag{11}$$

The geodesic connection between shapes is computed by defining the controlling vector fields to minimize the norm between the flowed shape and the target shape. The optimal control generating the geodesic connection between two shapes, minimizes the running cost with initial condition $q_0 = q_{\text{init}}$ and target endpoint condition, is given by the following:

Variational Problem

$$\min_{\substack{\boldsymbol{u}:\dot{\boldsymbol{\varphi}}_t = \boldsymbol{u}_t \circ \boldsymbol{\varphi}_t \\ \boldsymbol{\varphi}_0 = id, \boldsymbol{\mu}_t = \boldsymbol{\varphi}_t \cdot \boldsymbol{\mu}}} \int_0^1 \sum_\ell \|u_t^\ell - u_t^{\ell-1}\|^2_{V_\ell} dt + \|\boldsymbol{\mu}' - \boldsymbol{\mu}_1\|^2 \,. \tag{12}$$

The Pontryagin maximum principle provides necessary conditions for optimal solutions [8]. Hamiltonian control [8] reparameterizes the optimal control in what are termed momentum variables which act as Lagrange multipliers on the velocities to control the energy of the system. Define momentum $p_i^w, p_i^x = (p_{i1}^w, p_{i2}^w, p_{i3}^w), (p_{i1}^x, p_{i2}^x, p_{i3}^x)$ which act on the velocities $\dot{w}_i = w_i \text{div} u(x_i)$, $\dot{x}_i = u(x_i)$. The geodesics for Hamiltonian control for arbitrary kernels $G_\ell, \ell = 0, 1, \ldots$ for Reproducing Kernel Hilbert Space (RKHS) V_ℓ is now derived. Define the vector notation $u \cdot q = (u^\ell \cdot q^\ell)_{\ell\in L}$ for $p = (p^\ell)_{\ell\in L}$, $p^\ell = (p_i^{\ell,w}, p_i^{\ell,x}, p_i^{\ell,f})_{i\in I_\ell}$, with

$$u^\ell \cdot q^\ell = (\text{div}(u^\ell)(x_i^\ell) w_i^\ell, u^\ell(x_i^\ell), 0)_{i\in I_\ell}. \tag{13}$$

The Hamiltonian becomes

$$H(q,p,u) \doteq (p|u\cdot q) - \frac{1}{2}(\mathbf{L}u|u) \,, \tag{14}$$

with $(\mathbf{L}u|u) = \sum_{\ell\in L}(L^\ell v^\ell|v^\ell)$ with $(L^\ell v^\ell|v^\ell) = \|u^\ell - u^{\ell-1}\|^2_{V^\ell}$. The boundary term for matching in terms of the state $U(q_1) := \|\boldsymbol{\mu}' - \boldsymbol{\mu}(q_1)\|^2$ gives

$$p_{1i}^{\ell,w} = -\frac{1}{2}\frac{\partial}{\partial w_i^\ell} U(q_1), \tag{15a}$$

$$p_{1i}^{\ell,x} = -\frac{1}{2}\nabla_{x_i^\ell} U(q_1) \,. \tag{15b}$$

Here, to compute the optimal value of u given q and p, it may be convenient to introduce for $l \geq 0$, the mapping $u \mapsto (\delta_x^A|u)$ from $\mathcal{C}_0^l(\mathbb{R}^d, \mathbb{R}^d)$ (the space of $\mathcal{C}^l$ vector fields vanishing at the infinity) to $\mathbb{R}$ defined for $A \in L_l(\mathbb{R}^d, \mathbb{R}^d)'$ (the dual of the space of l-multilinear mappings on $\mathbb{R}^d$ with values in $\mathbb{R}^d$) and $x \in \mathbb{R}^d$ as

$$(\delta_x^A|u) \doteq (A|d^k u(x)) \,. \tag{16}$$

We get $p_i^w \text{div}(u^\ell)(x_i^\ell) w_i^\ell = p_i^w (\delta_{x_i^\ell}^{I_2}|u^\ell) w_i^\ell$ and $(p_i^{\ell,x}|u^\ell(x_i)) = (\delta_{x_i^\ell}^{p_i^{\ell,x}}|u^\ell)$ so that we deduce

$$\begin{aligned} v^\ell &= K^\ell \left(\textstyle\sum_{m\geq\ell} \sum_{i\in I^m} (p_i^{m,w} w_i^m \delta_{x_i^m}^{I_2} + \delta_{x_i^m}^{p_i^{m,x}}) \right) \\ u^\ell &= \textstyle\sum_m \left((\sum_{k\leq \ell\wedge m} K^k)(\sum_{i\in I^m} p_i^{m,w} w_i^m \delta_{x_i^m}^{I_2} + \delta_{x_i^m}^{p_i^{m,x}}) \right) . \end{aligned} \tag{17}$$

The geodesic state and momentum equation can then be derived from the Hamiltonian:

$$\begin{aligned} \dot{q} &= \tfrac{\partial}{\partial p} H(q,p,u) = u \cdot q, \\ \dot{p} &= -\tfrac{\partial}{\partial q} H(q,p,u) \,. \end{aligned} \tag{18}$$

For the evolution of the momentum, this gives

$$\begin{aligned} \dot{p_i}^{\ell,w} &= -(p_i^{\ell,w} \delta_{x_i^\ell}^{I_2}|u^\ell), \\ \dot{p_i}^{\ell,x} &= -\nabla_{x_i^\ell} \left(p_i^{\ell,w} w_i^\ell \delta_{x_i^\ell}^{I_2} + \delta_{x_i^\ell}^{p_i^{\ell,x}} |u^\ell \right) . \end{aligned} \tag{19}$$

The core equality to get an explicit formula for the Hamiltonian evolution is given by the following equality: for $k, l \geq 0$, $A \in L_k(\mathbb{R}^d, \mathbb{R}^d)'$, $B \in L_l(\mathbb{R}^d, \mathbb{R}^d)'$ we have

$$(\delta_x^A|K\delta_y^B) = (A \otimes B|\partial_x^k \partial_y^l K(x,y)) \tag{20}$$

since for $\alpha \in \mathbb{R}^{d'}$, $(\alpha|(K\delta_y^B)(x)) = (\delta_x^\alpha|K\delta_y^B) = (\delta_y^B|K\delta_x^\alpha) = (B \otimes \alpha|\partial_y^l K(y,x))$ so that $(\delta_x^A|K\delta_y^B) = (B \otimes A|\partial_x^k \partial_y^l K(y,x)) = (A \otimes B|\partial_x^k \partial_y^l K(x,y))$. In particular we have (using Einstein summation convention on

repeated indices):

$$\left\{\begin{array}{l} \partial_{x^a}(\delta_x^{I_2}|\delta_y^{I_2}) = \partial^3_{x^a,x^b,y^c} K(x,y)^{b,c}\,, \\ \partial_{x^a}(\delta_x^{I_2}|\delta_y^{\beta}) = \partial_{x^a}\partial_{x^b} K(x,y)^{b,c}\beta_c \\ \partial_{x^a}(\delta_x^{\alpha}|\delta_y^{\beta}) = \partial_{x^a} K(x,y)^{b,c}\alpha_b\beta_c, \\ \partial_{x^a}(\delta_x^{\alpha}|\delta_y^{I_2}) = \partial_{x^a}\partial_{y^c} K(x,y)^{b,c}\alpha_b \end{array}\right. \tag{21}$$

from which we can implement the Hamiltonian flow given the kernel.

5. Conservation laws

We consider $\boldsymbol{A} : \prod_{\ell\in L} V^{(\ell)} \to \prod_{\ell\in L} C_0^{k+2}(\mathbb{R}^d,\mathbb{R}^d)$ a continuous linear mapping. If we denote $|\boldsymbol{v}|_V^2 = \sum_{\ell\in L}|v^{(\ell)}|^2_{V^{(\ell)}}$, our construction leads to the Hamiltonian $\boldsymbol{\mathcal{H}}$ on $\prod_{\ell\in L} C_0^k(\mathbb{R}^d,\mathbb{R}^d)^* \times \prod_{\ell\in L} C^k_{Id}(\mathbb{R}^d,\mathbb{R}^d) \times \boldsymbol{V}$:

$$\begin{aligned} \boldsymbol{\mathcal{H}}(\boldsymbol{p},\boldsymbol{\varphi},\boldsymbol{v}) &= (\boldsymbol{p}|\boldsymbol{u}.\boldsymbol{\varphi}) - \frac{1}{2}(\boldsymbol{L}\boldsymbol{v}|\boldsymbol{v}) \\ &= \sum_{\ell\in L}(p^{(\ell)}|u^{(\ell)}\circ\varphi^{(\ell)}) - \frac{1}{2}\sum_{\ell\in L}|v^{(\ell)}|^2_{V^{(\ell)}}\,. \end{aligned} \tag{22}$$

where $\boldsymbol{u} = \boldsymbol{A}\boldsymbol{v}$ with $u^{(0)} = v^{(0)}$ and $u^{(\ell)} = v^{(\ell)} + u^{(\ell-1)}$ for $\ell \geq 1$. Since $\boldsymbol{\mathcal{H}}$ is $\mathcal{C}^2$ with bounded derivatives, we have a global solution for the Hamiltonian equation for any initial conditions $(\boldsymbol{\varphi}_0, \boldsymbol{p}_0)$ and since $\boldsymbol{\mathcal{H}}$ is right invariant, we get a conservation equation from Noether's theorem so that for any $\ell \in L$ we have the conservation equation, for any $w \in C_0^k$,

$$\frac{d}{dt}(\mathfrak{m}_t^\ell|(d\varphi_t^{(\ell)}w)\circ(\varphi_t^\ell)^{-1}) = 0\,, \tag{23a}$$

where $\mathfrak{m}^\ell$ is given by Hamiltonian momentum

$$(\mathfrak{m}_t^{(\ell)}|w) = (p_t^{(\ell)}|w\circ\varphi_t^{(\ell)})\,. \tag{23b}$$

For particles, $\mathfrak{m}$ are delta-Dirac generalized functions, defined in terms of their action against test functions w. For a classical density function, then $p^\ell = \mathfrak{m}^\ell\circ\varphi^\ell|d\varphi^\ell|$ with

$$\begin{aligned} \mathfrak{m}^\ell &= (L^\ell + L^{\ell+1})u^\ell - L^{\ell+1}u^{\ell+1} - L^\ell u^{\ell-1} \\ &= L^\ell v^\ell - L^{\ell+1}v^{\ell+1} \end{aligned} \tag{24}$$

For the more general case,

$$\mathrm{Ad}^*_{\varphi_t^{(\ell)}}(\mathfrak{m}_t^{(\ell)}) = \mathrm{Cte} \tag{25a}$$

$$\text{or}\quad \dot{\mathfrak{m}}_t^{(\ell)} + \mathrm{ad}^*_{u_l^{(\ell)}}(\mathfrak{m}_t^{(\ell)}) = 0\,, \tag{25b}$$

with $(\mathrm{ad}^*_u(\mathfrak{m})|w) = (\mathfrak{m}|Du\,w - Dw\,u)$, $\boldsymbol{u} = \boldsymbol{A}\boldsymbol{v}$ and $\boldsymbol{v} = \boldsymbol{K}\boldsymbol{A}^*\mathfrak{m}$, and $u^{(\ell)} = \sum_{k\leq m, k\leq\ell} K^{(k)}\mathfrak{m}_t^{(m)}$.

6. Results

Figure 2 depicts the micro scales of histological measurement that we are obtaining for studying Alzheimer's disease. This data is being mapped to the millimeter anatomical scales at moderate and high field MRI [13]. Each tau tangle (brown structure) is represented as a point particle that carries a location (here a position in 2 dimensions) and a functional signal (here its cross sectional area).

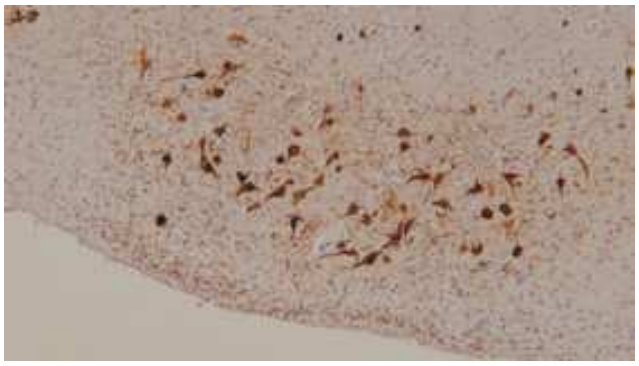

Figure 2: Micron scale histology image of a slice of tissue from the medial temporal lobe of the brain, stained for tau tangles (brown).

Our implementation is based on a two layer hierarchy. At the fine scale, a varifold represents individual particles (tau tangles) with a one dimensional functional signal describing their size, and weights w set to 1. At the coarse scale, the varifold includes particles sampled on a regular grid, with a two dimensional functional signal that describes local mean and local standard deviation of the fine scale particle size, and weights set to the local density of fine scale particles. Optimal flows to match a template to a target varifold were computed by minimizing our Variational Problem (12) over velocity fields sampled on a regular grid. Minimization was performed using automatic gradient calculations in pytorch, with gradient descent.

We first show one simulated example, illustrated in Fig. 3. The first row shows individual particles at the finest scale. Marker size is proportional to their weights, and marker color shows their functional signal. This example shows a template and target that are simple squares with "large" signal on the left, and "small" signal on the right. The template particles (left column) are transformed (center column) to match the target particles (right column) under the flow $v^0 + v^1$. In addition to changing position, they also change weight (illustrated by size) as described in (2). The second and third row show a coarse scale varifold representation where features are local mean and local standard deviation (respectively). From left to right the local mean

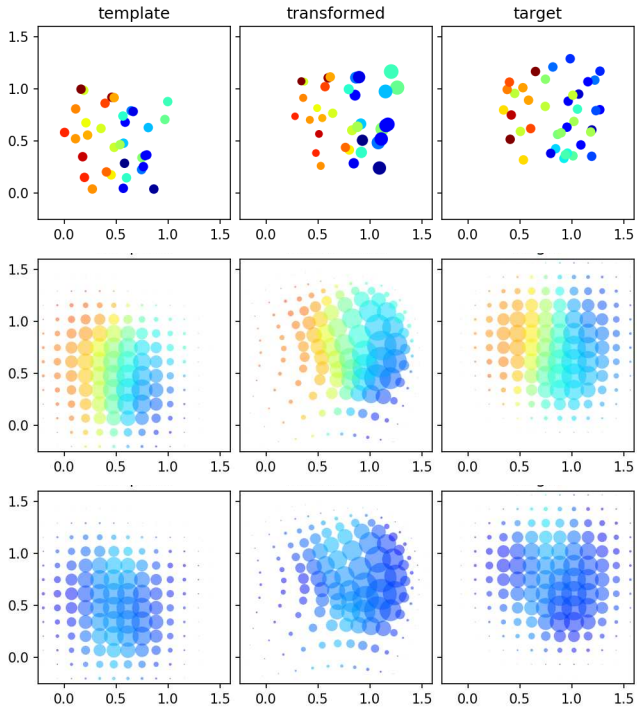

Figure 3: Varifold representation of simulated data, where color represents signal and size represents weight. The template (left) is transformed (center) to match the target (right). Particles are shown at fine scale (top), and coarse scale with local mean (middle) and local standard deviation (bottom).

changes from red to blue, and the standard deviation is high in the transition zone between them.

The initial velocity fields corresponding to this optimal flow are shown in Fig. 4. Here the velocity field's magnitude is shown as a grayscale image, and its direction is shown by arrows at several sampled points. The coarse scale controls an average change in position, whereas the fine scale controls placement of individual particles as well as changes in weight through its relatively large divergence.

Second, we show an example using tau tangles that were detected in the histology image of Fig. 2, where the functional signal carried by each particle is its size. We analyze the collateral sulcus, a region which begins to accumulate tau tangles in the earliest stages of Alzheimer's disease. Corresponding varifolds are illustrated in Fig. 5, where local statistics are computed using a Gaussian neighborhood of 20 pixels. Each tau tangle, visible as a brown particle at a zoomed in scale in Fig.2, corresponds to a single marker in the top row of Fig. 5. We note that by analyzing local mean, a gradient of small tangles in superficial layers to large tangles in deep layers is observed on the lateral bank of the

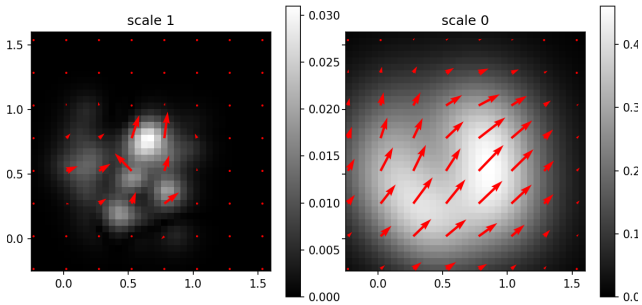

Figure 4: Initial velocity fields at fine and coarse scales for simulated example. Magnitude is shown in grayscale and red arrows indicate direction.

collateral sulcus.

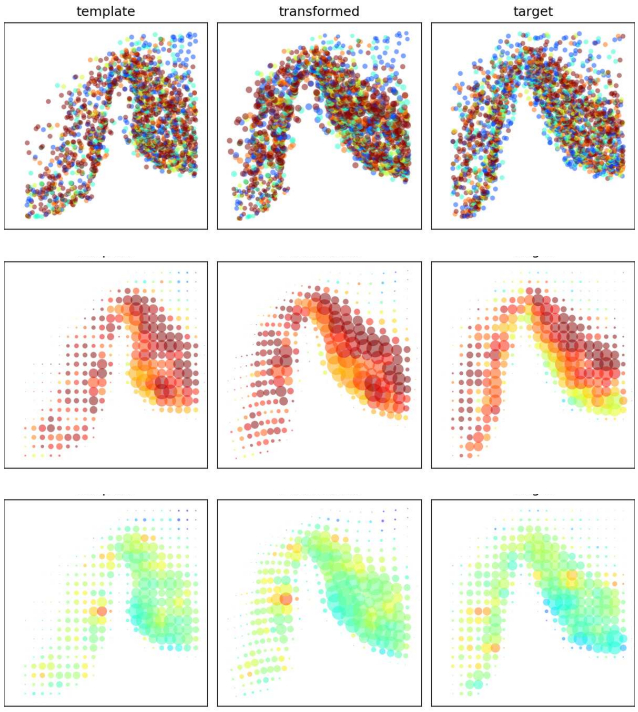

Figure 5: Varifold representation of tau tangle data, where marker color represents tangle size, and marker size represents weight. The template (left) is transformed (center) to match the target (right). Particles are shown at fine scale (top), and coarse scale with local mean (middle) and local standard deviation (bottom).

The initial velocity fields corresponding to the optimal flow for the histology example are shown in Fig. 6. Here the velocity field's magnitude is shown as a grayscale im-

age, and its direction is shown by arrows at several sampled points. Velocity fields are smoothed by Green's kernels of the operator $(id - a^2\Delta)^4$ with Δ the Laplacian and $a = 20$ (for coarse scale) and 5 (for fine scale) pixels. Here we see that the fine scale encodes flows of much smaller magnitude (by a factor of 10) than the coarse scale, as expected for its interpretation as a refinement. The fine scale includes a large divergence that modifies particle weight in addition to a refinement in position.

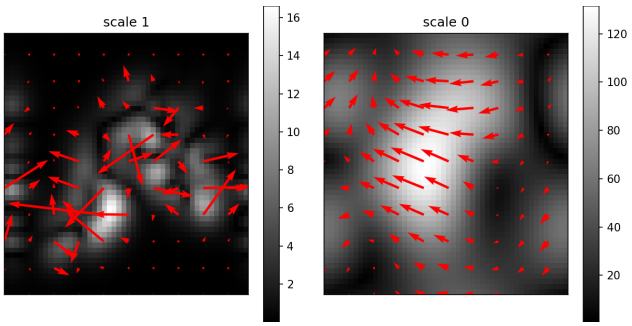

Figure 6: Initial velocity fields at fine and coarse scales for histology example. Magnitude is shown in grayscale and red arrows indicate direction.

7. Conclusion

In this work we presented a new approach to modeling anatomical form at multiple spatial scales. We used varifolds to model individual particles such as cells expressing functional signals, as well as to model coarser features such as local means and standard deviations. We modeled shape differences through the action of diffeomorphisms, generated from flows at different scales, with an associated metric. In this setting, we derived an optimal Hamiltonian control which describes geodesics in our shapespace, and showed one simulated example, and one example from digital pathology, of shape matching.

Biomedical images, such as those seen in digital pathology, are increasing in size and resolution. Models that can describe cells or particles at fine scales, and continuous data at coarse scales, are becoming necessary. The approach we have presented here extends the techniques of Computational Anatomy into this important setting.

References

[1] R.A. Akansu, A.N.; Haddad. *Multiresolution signal decomposition: transforms, subbands, and wavelets*. Academic Press, 1992. 1

[2] Peter J. Burt and Edward H. Adelson. The laplacian pyramid as a compact image code. *IEEE TRANSACTIONS ON COMMUNICATIONS*, 31:532–540, 1983. 1

[3] Ingrid Daubechies. *Ten Lectures on Wavelets*. Society for Industrial and Applied Mathematics, USA, 1992. 1

[4] Barbara Gris, Stanley Durrleman, and Alain Trouvé. A sub-riemannian modular framework for diffeomorphism-based analysis of shape ensembles. *SIAM Journal on Imaging Sciences*, 11(1):802–833, 2018. 1

[5] Brian C. Lee, Daniel J. Tward, Partha P. Mitra, and Michael I. Miller. On variational solutions for whole brain serial-section histology using a sobolev prior in the computational anatomy random orbit model. *PLOS Computational Biology*, 14(12):1–20, 12 2018. 1

[6] Stphane Mallat. *A wavelet tour of signal processing (2. ed.)*. Academic Press, 1999. 1

[7] Stphane Mallat. Group invariant scattering. *Communications on Pure and Applied Mathematics*, 65(10):1331–1398, 2012. 1

[8] Michael I Miller, Alain Trouvé, and Laurent Younes. Hamiltonian systems and optimal control in computational anatomy: 100 years since d'arcy thompson. *Annual Review of Biomed Engineering*, (17):447–509, November 4 2015. 3

[9] Marc Niethammer, Roland Kwitt, and Francois-Xavier Vialard. Metric learning for image registration. In *Proceedings of the IEEE Conference on Computer Vision and Pattern Recognition*, pages 8463–8472, 2019. 1

[10] Laurent Risser, François-Xavier Vialard, Robin Wolz, Maria Murgasova, Darryl D Holm, and Daniel Rueckert. Simultaneous Multi-scale Registration Using Large Deformation Diffeomorphic Metric Mapping. *IEEE Transactions on Medical Imaging*, 30(10):1746–59, 2011. 1

[11] N Sacktor, A Soldan, M Grega, Farrington L, Q Cai, MC Wang, RF Gottesman, RS Turner, Albert M, and BIOCARD Research Team. The biocard index: A summary measure to predict onset of mild cognitive impairment. alzheimer dis assoc disord. *Alzheimer Disease Association Disord*, 31(2):114–119, Apr-Jun 2017. 1

[12] Stefan Sommer, Mads Nielsen, François Lauze, and Xavier Pennec. A multi-scale kernel bundle for LDDMM: towards sparse deformation description across space and scales. *Information processing in medical imaging proceedings of the conference*, 22(17):624–635, 2011. 1

[13] Daniel Tward, Timothy Brown, Yusuke Kageyama, Jaymin Patel, Zhipeng Hou, Susumu Mori, Marilyn Albert, Juan Troncoso, and Michael Miller. Diffeomorphic registration with intensity transformation and missing data: Application to 3d digital pathology of alzheimer's disease. *Frontiers*. 1, 4

[14] Daniel Tward, Xu Li, Bingxing Huo, Brian Lee, Partha Mitra, and Michael Miller. 3d mapping of serial histology sections with anomalies using a novel robust deformable registration algorithm. In *Multimodal Brain Image Analysis and Mathematical Foundations of Computational Anatomy*, volume LNCS, volume 11846, October 10 2019. 1

[15] F-X Vialard, L Risser, D Rueckert, and CJ Cotter. 3d image registration via geodesic shooting using and efficient adjoint calculation. *Journal International Journal of Computer Vision*, 97(2):229–241, April 2012. 1